Theoretical concept for in-situ condition monitoring of rotary shaft seals using surface strain-based analysis of the deformation state

Y. Stiemcke, S. Thielen, O. Koch

Abstract

In situ condition monitoring of rotary shaft seals could significantly improve the reliability of future seals in numerous applications. A superficial application of strain gauges capturing the state of deformation could offer a cost-effective retrofit solution for indirect measurements of central operational parameters. Within a simulative investigation of the sealing system, possible sensor positions for determination of the preload as well as the friction torque prevailing in the sealing contact are therefore identified as two parameters directly related to the operating condition. Further investigations of the potential sensor signal with focus on its time-dependent behavior prove the theoretical feasibility of the measurement concepts developed and provide promising prospects for an initial technical implementation.

Theoretische Konzeption einer in situ Zustandsüberwachung an Radialwellendichtringen anhand oberflächendehnungsbasierter Erfassung des Deformationszustands

Zusammenfassung

Eine in situ Zustandsüberwachung an Radialwellendichtringen könnte zukünftig die Zuverlässigkeit von Abdichtungen in zahlreichen Anwendungen deutlich verbessern. Eine oberflächliche Applikation von Dehnungsmessstreifen für Erfassungen des Deformationszustands könnte dabei eine kostengünstige Nachrüstlösung zur indirekten Messung zentraler Betriebsgrößen bieten. Im Rahmen einer simulativen Untersuchung des Dichtsystems werden daher mögliche Sensorpositionierungen zur Bestimmung der Vorspannung sowie des im Dichtkontakt vorherrschenden Reibmoments als zwei direkt mit dem Betriebszustand zusammenhängende Parameter identifiziert. Weiterführenden Untersuchungen des potenziellen Messsignals mit Fokus auf dessen zeitabhängiges Verhalten belegen dabei die theoretische Machbarkeit der entwickelten Messkonzepte und liefern vielversprechende Ausblicke auf eine erste praktische Umsetzung.

✉ Y. Stiemcke
yvo.stiemcke@rptu.de

1   Chair of Machine Elements, Gears and Tribology (MEGT)
     University of Kaiserslautern-Landau (RPTU)
2   Gottlieb-Daimler-Straße, Building 42, 67663 Kaiserslautern, Germany

1   Motivation and state of the art

Until recently, machine elements such as shaft seals or bearings mainly had to fulfill their primary role (e.g. in the case of shaft seals to seal the exit of a rotating shaft from a lubricated machine). In recent years, advances in microelectronics, mainly driven by consumer products, have made microelectronic sensors and communications modules much smaller and more cost efficient. These developments enable the manufacturers of machines and also their individual components to integrate sensor functions in their products to allow for a better monitoring of their operational state and condition [1]. Since they are typically standardized in their outer dimensions and functional properties, such an integration of sensor functions in machine elements poses a significant challenge. In many cases, their use inside a lubricated machine with highly optimized installation spaces does not allow for a cable based connection providing communication and energy supply. Therefore, the integration of such functions must be neutral regarding the installation. Furthermore, the application of sensors and other microelectronic components can possibly influence the load capacity or functional properties of the machine element. This results in the need for design calculation methods that allow to take these influences into account.

In this paper, we present a simulative study of radial shaft seals (RSS) with the goal of finding the ideal placement for strain gauges meant to facilitate the determination of the friction torque during seal operation and the relaxation of the seals radial force during operation. This work is part of a bigger project aiming at showing the feasibility of measuring different operational states and properties of shaft sealing systems [2].

RSS are typically used to seal off the exit of rotating shafts from lubricated machinery, such as gearboxes or rotor bearing units [3] [4]. Besides keeping the lubricant inside the machine [5] [6], they also must prevent environmental contamination such as water or dirt from entering the machine. In almost all applications, they are designed to match or exceed the service life of the machine in order to prevent costly replacements.
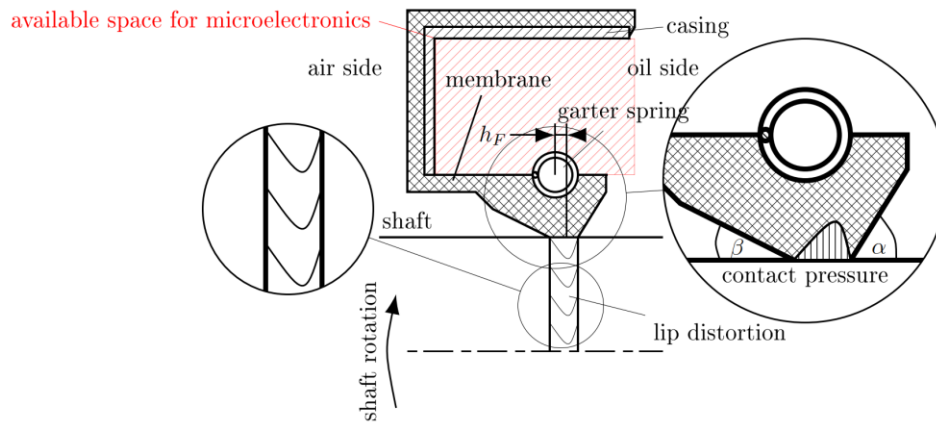

Figure 1: Cross section of a radial shaft seal and illustration of aspects of its sealing mechanism. Red: Available dead space that can be used to integrate micro-electronics

RSS consist of a rubber part vulcanized on a metal casing which is meant to be fit into the seal bore (Figure 1). The rubber part consists of a membrane, the sealing lip and a notch for a garter spring. During installation of the seal on the shaft, the sealing lip is widened since its inner diameter is smaller than the shaft diameter. The difference between both is called interference. The membrane allows the sealing lip to widen and tilt during this process and also provides flexibility for the seal to follow shaft runout and other misalignments. Due to the widening of the sealing lip, a contact pressure (pre-load) is created between the shaft surface and the sealing lip. The contact pressure is further reinforced by the use of a garter spring, which is meant to provide a minimal contact pressure during high operation temperatures which soften the rubber and thereby reduce the fraction of the contact pressure provided by the stretching of the rubber part. The shape of the contact pressure distribution in an axial cross section must be asymmetrical with its maximum closer to the oil side in order to allow for an active sealing mechanism. This is achieved by choosing a flat contact angle (beta) on the air side, a more acute angle on the oil side and in addition also by positioning the plane of action of the garter spring slightly towards the air side in relation to the contact area between sealing lip and shaft (c.f. h_f in Figure 1). The contact pressure between lip and shaft must be high enough to allow the sealing mechanism. Therefore, the radial force of the seal, which is the overall contact force between seal and shaft has become an important metric for the function of RSS, which can be evaluated in the new condition and also after use in the worn state where the radial force is typically diminished by wear and changes in the mechanical properties of the rubber.

While the sealing effect during standstill is based on the deformation of the rubber lip against the shaft surface and consequently a closure of percolation channels for the lubricant [7], during shaft rotation a lubricant film is formed between rubber lip and shaft. The friction torque resulting from the rotation distorts the rubber lip in circumferential direction, creating a v-shaped distortion of the roughness structure on the sealing lip (c.f. Figure 1). Due to the different contact angles, the length of the air side distortion structure is longer than on the oil side. The lubricant which is dragged in circumferential direction by the shaft rotation is partly conveyed in axial direction by those distorted structures. Due to its length, the conveyance effect on the oil side directed towards the air side dominates resulting in a net conveyance of oil from air to oil side. This constitutes the active sealing mechanism of RSS during shaft rotation.

Since this process depends on a significantly high contact pressure between shaft and seal, RSS typically also have a comparably high friction torque. The resulting frictional power loss furthermore is concentrated on the very small contact area between seal and shaft, resulting in significant overtemperatures [8]. Consequently, the knowledge of the friction torque of an RSS during operation can provide significant insights in the seals function and can also help to identify critical operational states and also the condition of the seal. The same is also true for the pre-load of the seal. Therefore, in the context of research projects and also industrial testing, several test benches for determining the friction toque of RSS exist [8] [9] [10] [11] [12]. While those test benches either measure the reaction torque of the test cell or the driving torque of the drive shaft, there exists no possibility of measuring the friction torque

from within the seal itself yet. Consequently, the friction torque of RSS in commercial machines is not yet accessible to the users or manufacturers, although they could possibly benefit from having this data available.

Due to the relatively large area of the unused space between the metal casing and the rubber membrane, lip and garter spring (red hatched area in Figure 1), the RSS has the potential for the installation of various microelectronic components without affecting its outer dimensions. This would also allow the placement of strain gauges at strategic positions on the RSS, chosen in a way that they allow the measurement of strain induced by the assembly / pre-load and also by the friction torque. In order to find the ideal placement of such strain gauges, a simulative study of the strain on the surface of the RSS produced by the aforementioned effects need to be conducted.

2   Material behavior of rubber

The requirements for a simulative strain analysis are derived from the rubber material properties. Due to numerous influences associated with the material behavior, assumptions made during modeling must always be compatible with the aim of the investigation. The material properties to be described are primarily characterized by high deformability under low stresses [13]. For quasi-static structural-mechanical problems, such as a simulative sensor placement, hyperelastic material modeling according to MOONEY-RIVLIN offers a suitable approach commonly used in technical applications [14]. This phenomenological approach for initially isotropic and incompressible rubber [15] derives a non-linear stress-strain relationship from the general strain energy density function W [16] according to equation (1).

$$W = C_{01}(I_1 - 3) + C_{10}(I_2 - 3) \tag{1}$$

Here, the deformation of a volume element is described independently of the coordinate base by the first two invariants of the CAUCHY-GREEN tensor I_1 (change in length of the spatial diagonals) and I_2 (change in surface area) [17]. Equation (1) thus provides a mathematical description of the non-linear elastic modulus based on the empirical material coefficients C_{01} and C_{10}, which can, for example, be obtained from uniaxial tensile tests [18]. In combination with a sample conditioning the characteristic temperature dependency of the material behavior [13] can also be considered. The MOONEY-RIVLIN model thus provides an approximation of the strain-dependent stress usable in the finite element method (FEM) for numerous operating conditions and technical strains of up to 80% [19].

In cases of changing deformations or interest in the time-dependent system behavior, such as the examination of a potential measurement signals intended for this study, the MOONEY-RIVLIN approach represents no suitable model, since rubbers in reality furthermore exhibit a stress state strongly dependent on time and load history [14]. As a consequence, the material is subject to a progressive loss of stress called relaxation when constant strain is applied (displacement-controlled deformation). In contrast, when constant stress is applied (force-controlled deformation), a time delay occurs in strain build-up, known as retardation. The resulting time-dependent resilience is termed creep and develops in proportion to prevailing stress [20]. A phenomenological description of the abovementioned mechanisms follows from the theory of linear viscoelastic deformation behavior for sufficiently low stresses and strains [20]. This theory is fundamentally based on the BOLTZMANN superposition principle, which assigns a stress state prevailing in the material to the linear superposition of past deformations [21]. In this context, the influence of a past deformation on the current state diminishes with the time elapsed since its occurrence according to the principle of fading memory [22].

A linear viscoelastic material behavior can be described mathematically by the generalized MAXWELL model (c.f. Figure 2), which can be visualized as a parallel connection of a spring with several MAXWELL elements (each series connection spring with elastic modulus E_i and damper of viscosity η_i) [21].
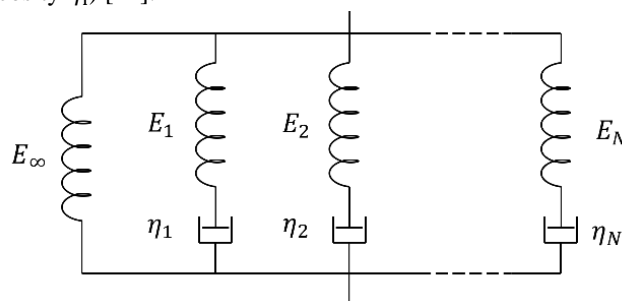

Figure 2: Visualization of the generalized MAXWELL model as a parallel connection of spring and spring-damper elements

While the rubbers's long-term behavior is represented by the stand-alone elasticity drawn left in Figure 2 (elastic modulus E_∞), the dynamic component is given by the combination of N MAXWELL elements, which each exhibit an individual exponential time dependency [18]. According to equation (2) the total time-dependent elastic modulus E(t) therefore results from the sum of the long-term value E_∞ and the superimposed MAXWELL elements [23].

$$E(t) = E_\infty + \sum_{i=1}^{N} E_i * e^{-\frac{t}{\tau_i}} \tag{2}$$

In practice, a parameter determination for equation (2) is often based on the harmonic excitation of specimen at varied frequency [21]. An additional consideration of the sample temperature as a test parameter within the scope of a dynamic mechanical thermal analysis (DMTA) furthermore enables the quantification of the material parameters' temperature dependency as well as a determination of relaxation and retardation spectra over extended time periods [24]. The spectrum can then be approximated by an Nth order PRONY series according to equation (2), where each MAXWELL element represents a separate time interval τ_i [14]. If at least one member of the series is parameterized for each time decade, the time-dependent material behavior is described with sufficient accuracy [14] and can be used in transient FE simulation approaches.

3   Structural analysis

The foundation for sensor placement and the theoretical development of a measurement concept (c.f. Section 4) is an in-depth investigation of the operational state-dependent RSS deformation. This system behavior is generated using the simulation model presented in this chapter (Section 3.1) and evaluated as subsequently demonstrated (Section 3.2).

3.1   Simulation model of the sealing system

The determination of suitable strain gauge placements on the sealing lip of the RSS (Type BAUM5X7 80-100-10) are carried out based on its replication as a parametric FE model in the simulation environment ABAQUS CAE (Python Scripting Interface). Following the work of BURKHART [24] [25] a cross-section geometry-based model [26] is used undertaking adaptations for three-dimensional examinations of deformation due to assembly and shaft rotation.

The resulting configuration, consisting of a metal case, rubber body and garter spring acting as firmly connected components together with a hollow shaft serving as a counter surface, can represent the sealing system in high resolution by utilization of its rotational symmetry with a revolution angle of 2°. The segment model shown in Figure 3 is used to analyze the RSS surface strain as it is relevant for sensor placement (Section 4.1, Section 4.2) and predictions about potentially measurable quantities (Section 4.3). For this purpose, the assembled state (II) as well as operational condition (III) are simulated according to the sequence described below in order to read out the 3x3 strain tensor along the center profile highlighted in red and derive the deformation parameters described in Section 3.2.
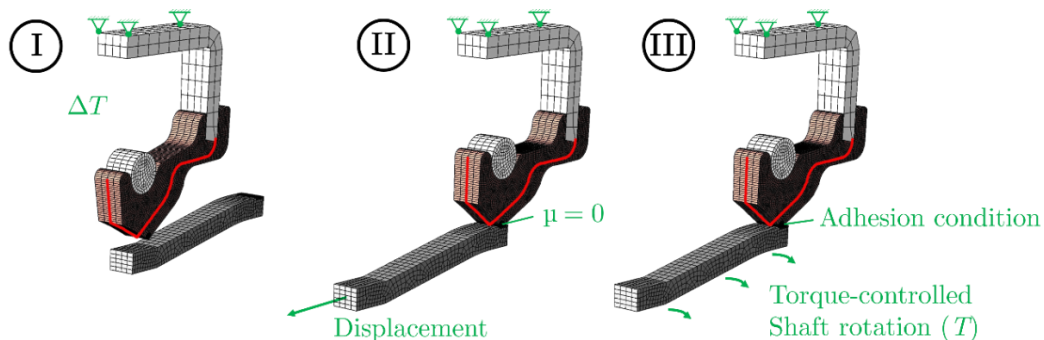

Figure 3: Segment model in cyclic symmetry for operating point-dependent evaluation of surface strain states

Next to the definition of a cyclic symmetry as repetitive interaction between both cut surfaces the circumferential surface of the metal case is initially (state I in Figure 3) fixed corresponding to the press fit in the seal bore. The prevailing temperature distribution is simplified to room temperature (initial condition: 22°C, homogeneous) since the fundamental development of a metrological approach stands in the focus of this investigation.

During the assembly process, the axially displaced shaft gets into contact with the sealing lip under the assumption of absence of tangential friction. Due to the resulting assembly deformation in state II, a contact pressure occurs (compare Section 1), which is partly caused by a widening of the inner sealing lip diameter. Here, a fully hyperelastic material model implemented for sensor placement displays the long-term behavior of the rubber (75 FKM 585) and thus the largest occurring deformation, so that the interference-induced radial force shows no time dependency due to relaxation processes [27] [28]. A contact pressure reinforcement caused by the garter spring is further modeled by way of a diameter-dependent spring force [29]. A model validation can therefore be carried out, as shown in Table 1, by a comparison of contact parameters read out in state II with measurements of a batch of 20 RSS of the simulated design. As reference values the radial force acquired according to the two-jaw method [30] as well as contact width and angles obtained from profilometric measurements [31] are considered each at room temperature.

	Radial force / N	Contact width / μm	Contact angle α / °	Contact angle β / °
Measurement	31.4	91.0	38.5	24.3
Simulation (state II)	31.1 (-1.0%)	99.5 (+9.3%)	36.2 (-6.0%)	23.5 (-3.3%)

Table 1: Model validation based on measured contact parameters at room temperature averaged over 20 RSS

The now validated assembly state (II) is followed by the operational state (III) of the sealing system. In this step an adhesion condition is added to the contact and a controlled torque (friction torque T) applied on the countersurface leads to shaft rotation. Thus, a characteristic distortion state occurs in the rubber body in state III analogously to friction-induced deformation in case of continuous shaft rotation. The initially used material model according to MOONEY-RIVLIN results in strains representing the final state reached after a sufficiently long creep period ($t \rightarrow \infty$). Since the material behavior depending on time and any previous load history is expected to significantly influence on the surface strain to be measured (see Section 2), a second hyper-viscoelastic material model [24] is additionally implemented in selected simulations to derive the time-dependent course of potential measurement signals. Using the hyper-viscoelastic material model, relaxation as well as retardation mechanisms at the states II and III can be analyzed, which with increasing duration strive towards the final state of the quasi-static, fully hyperelastic material model.

3.2   Approach for simulation-based sensor placement

A prerequisite for the identification of possible sensor placements is knowledge of the strain state inside the RSS surface. Therefore, the 3x3 strain tensor read out along the profile (c.f. Figure 3) is first transformed at each node to its local coordinate system. The axes of these coordinate systems follow the edges of adjacent elements that intersect in the node representing the coordinate origin. Thus, all local coordinate systems are defined by the computational grid and are therefore able to adapt to prevailing deformations, such as the tilting of the sealing lip during the assembly process, as exemplary shown in Figure 4 for state II.
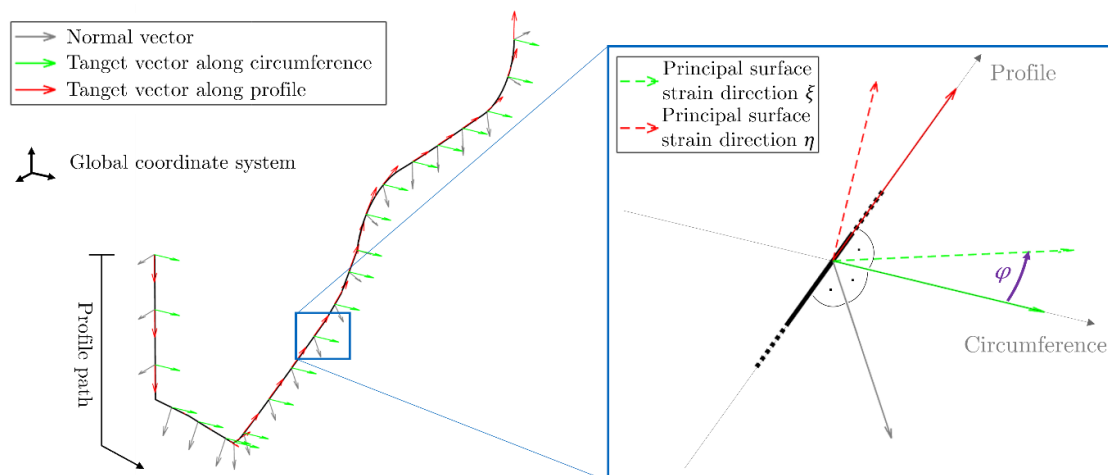

Figure 4: Transformation of the strain tensor into dynamic local coordinate systems (left) and principal directions of surface strain (right) schematic

As visualized in Figure 4 (left), the local coordinate axes describe the normal vector of the surface, as well as two tangent vectors along circumference and profile. Since applied strain gauges are exclusively affected by surface strains, the transformed strain tensor can be reduced by the normal vector and both associated shear components. The following analysis is therefore carried out considering a planar strain. From the remaining 2x2 tensor MOHR's strain circle [32] provides the total surface strain on the one hand, which must permanently fall below a maximum limit tolerable by the strain gauge as a necessary condition for possible placements (Section 4.1). On the other hand, the principal strain directions ξ und η, as illustrated in Figure 4 (right), are also determined in this way. Their position relative to the local coordinate system is described by the angle φ and serves to determine a suitable strain gauge alignment (Section 4.2). For further investigation (Section 4.3), surface strains occurring along the selected alignments are determined in the same manner and, using simplifying assumptions (neglected transversal contraction, influence of any bonding layer, stiffness of the carrier foil, etc.), evaluated as a potential measurement signal.

4   Derivation of the measurement concept

According to the method described all sections along the profile path can be evaluated regarding their suitability for a strain gauge application based on the long-term material behavior (Section 4.1) in order to select appropriate measuring grid orientations (Section 4.2). By means of hyper-viscoelastic simulation model the influence of the relaxation and creep behavior on the potential measurement signal is further investigated at selected positions and possible compensation opportunities (Section 4.3) are discussed.

4.1　Identification of technically feasible sensor placements and measurable operational parameters

For future implementation of the developed integration concept numerous suitable methods for piezoresistive strain measurement are available. These range from conventional foil strain gauges to temperature-independent thin-film solutions [33] and highly elastic strain gauge alternatives for soft systems [34], each of which involves individual requirements for the deformation body.

While the final sensor selection must be based not only on the achievable signal quality but also on practical experience in the future, such as reliability under various operating conditions, manufacturing limitations or critical mechanical interactions between sensor and sealing system, a prototype for the proof of functionality presented in the following part of this paper series will initially be realized using miniature foil strain gauges. These should preferably be attached to uncurved profile sections, which are marked in Figure 5 (left).
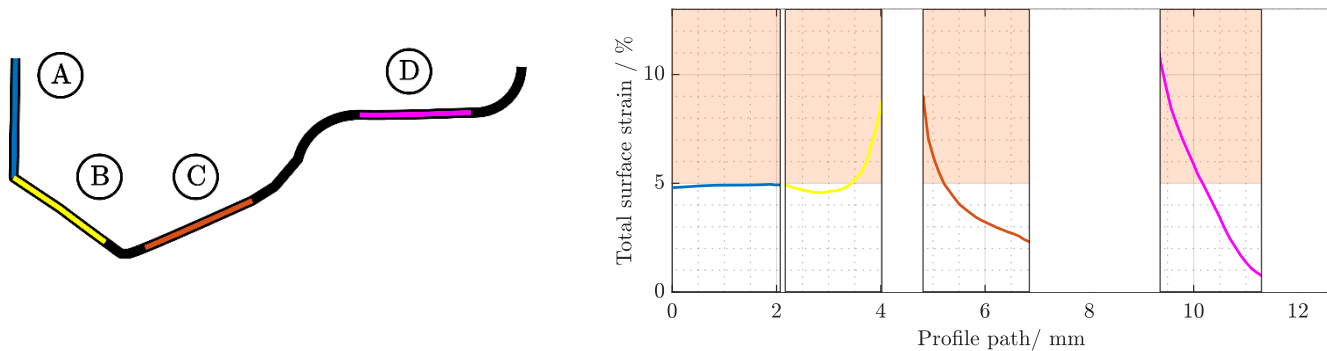

Figure 5: Total surface strain at worst-case operational state III ($T = 0.8$ Nm) on profile sections A-D potentially suitable for strain gauge application (left)

According to the worst-case operational conditions applied in Figure 5 (right), the total surface strain on all four sections falls entirely or over a sufficiently large area below the maximum strain of 5% that can be tolerated by the selected strain gauge. Thus, a durable strain gauge application could be possible there, although this requirement will also have to be assessed in future under boundary conditions of realistic operational scenarios. These particularly include the prevailing temperature field (sump, contact and environmental temperature) as an influence on the material behavior [24], differential pressures as a cause of intensified tilting of the sealing lip in connection with increased membrane deformation [35] as well as strain peaks due to dynamic shaft eccentricity. Should the above-mentioned influences lead to an exceedance of the strain limit, strain gauge application in a semi-deformed state, such as after mounting the RSS on a shaft below the nominal diameter, could increase the operational strain tolerance.

Furthermore, a high surface quality is required for sensor attachment, which, due to the manufacturing process of the RSS type considered, is given on the profile sections A, C and D (c.f. Figure 6, right).

$R_a^B = 1.44$ μm　　　$R_z^B = 6.96$ μm

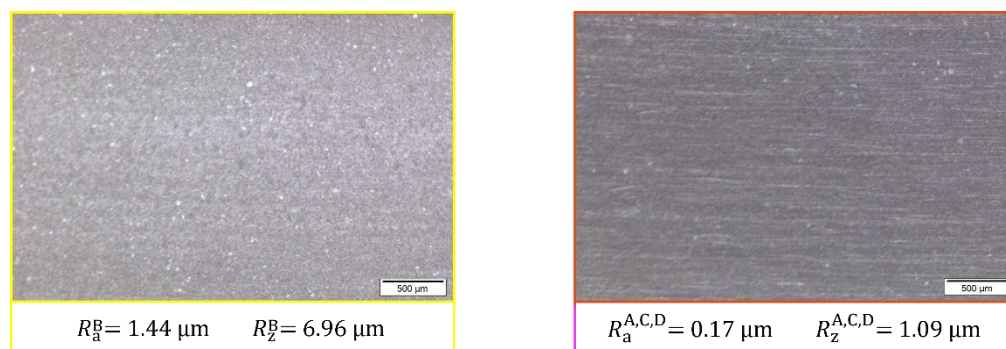$R_a^{A,C,D} = 0.17$ μm　　　$R_z^{A,C,D} = 1.09$ μm

Figure 6: Microscope image of cut-off oil sided lip face (left, section B) and untreated rubber surface (right, section C as example) as well as roughness parameters determined through confocal microscopy (mean values from 4 profiles distributed around the circumference)

In contrast, the air-sided lip face B differs from the others due to a machining step following the vulcanization process (Figure 6, left). As a consequence, a systematic roughness pattern with striking primary direction is shown here, which generally should be excluded on surfaces to be bonded [36]. Profile section B is therefore excluded as a potential sensor placement and sections A, C and D are considered.

Separating the surface strain components over the profile path in a comparison of assembly state II (Figure 7, left) with operational state III (Figure 7, right) now clearly indicates potentially measurable operational parameters in the remaining profile sections.
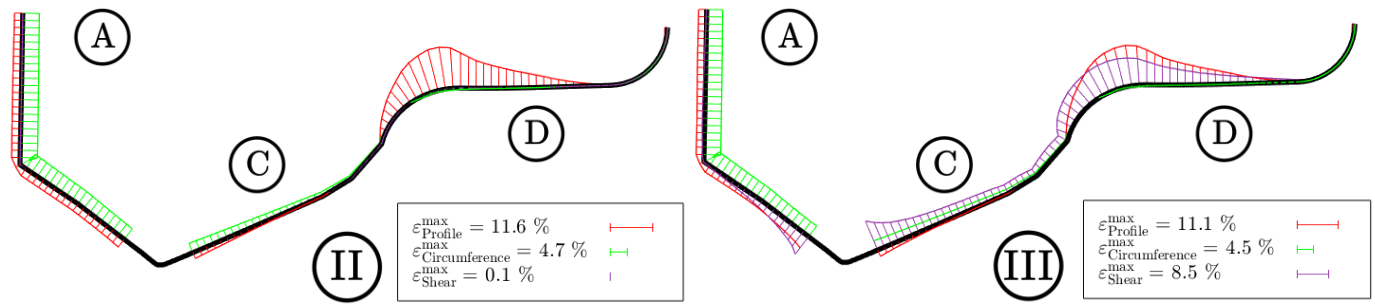
Figure 7: Components of the surface strain (2x2 tensor) in assembly state II (left) and worst-case operational state III ($T = 0.8$ Nm, right)

Profile section A shows a very constant surface strain along the profile section directed in the profile and circumferential direction, which persists almost unaffected by friction torque added in state III. Therefore, profile section A serves as a potential sensor placement providing strain measurements correlating with the sealing lip's preload connected to the radial force as well as the current state of relaxation (see Section 4.3) and thus provide in situ information about the rubber's ageing condition, wear or, in the case of high-frequency sampling, even losses of follow-up capability due to shaft runout as a known cause of leakage [37].

In opposite to this, the deformation occurring on the air-sided profile sections C and D under friction torque ($T = 0.8$ Nm) significantly contributes to the surface strain, whereby a pure shear component is added to the unaltered assembly deformation (see Figure 7, right). A strain gauge for friction torque measurement should preferably be installed on profile section C, since the ratio of torque-induced distortion as a target quantity to assembly deformation as a disturbance is greater here and therefore a better measurement signal can be expected. Additionally, profile section C according to Figure 5 offers a comparatively larger area below the strain limit of 5% as well as a lower local strain gradient, so that in the practical application lower demands are set on the strain gauge placement accuracy. Based on these observations, profile sections A and C are considered during the final sensor alignment and analysis of potential measurement signals in the following.

4.2 Strain gauge alignment and potential measurement signal

To achieve the best possible measurement signal, strain gauges should generally be oriented along the principal surface strain directions [38] [36], which can be determined as described in Section 3.2. The friction torque-dependent occurrence of both surface strain principals is characterized in Figure 8 by means of the total strain as their sum of magnitudes (each left-hand diagram) as well as their angle of appearance φ in relation to the local coordinate system (each right-hand diagram). Using the superposition principle [32], deformations due to operation in state III (shear deformation) is separated from the total deformation by compensating for the assembly deformation of state II.
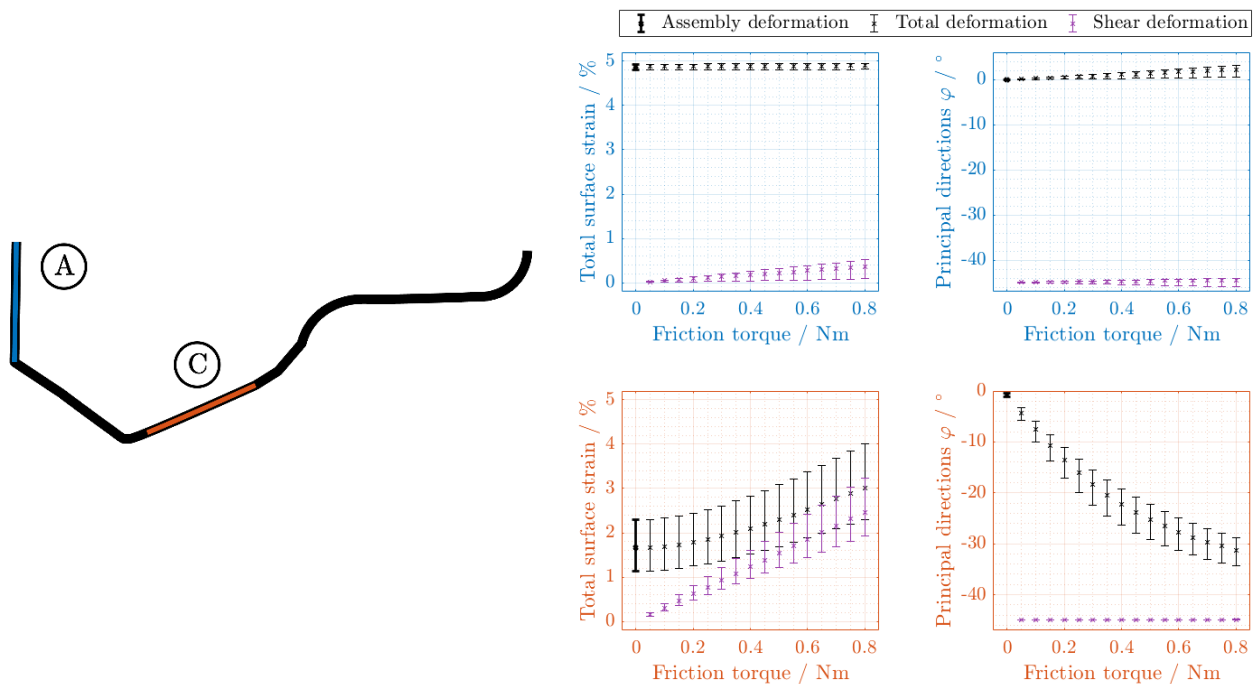

Figure 8: Total surface strain and rotation angle of the principal directions φ as a function of the friction torque T (visualization of the mean value over the profile sections marked on the left, as well as minimum and maximum as error bars)

Figure 8 demonstrates that the total deformation on the air-sided profile section C is dominated by the assembly state for low friction torque. With increasing friction torque, the additional shear component on the entire profile section (compare mean value, minimum and maximum shown as error bars in Figure 8) increases linearly, so that the total deformation strives towards the shear deformation. Since the initially prevailing assembly deformation, as known from Figure 7, proceeds exclusively in the profile and circumferential direction (principal directions $\varphi(0\,\text{Nm}) \approx 0°$), a superimposition with any shear deformation according to Figure 8 results in a torque-dependent rotation of the total strain tensor's principal directions. However, shear deformation-induced surface strains occur consistently at $\varphi \approx -45°$, so that the strain gauge serving primarily to determine the friction torque should be aligned according to this angle.

According to Figure 8, this approach will require compensation for the assembly deformation offset. Any offset shifts during operation which cannot be directly predicted by simulation, such as those caused by wear or material ageing, could potentially be compensated by strain alterations detected on the oil-sided profile section A. Here, the shear strain superposition described above occurs to a much smaller extent, so that a strain gauge orientation along the circumference ($\varphi = 0°$) is expected to provide the optimum signal quality.

Based on the defined sensor alignment, the long-term behavior ($t \to \infty$) of potential measurement signals, referred to in the following as measured long-term strain, can now be assessed (compare Section 3.2) as shown in Figure 9.
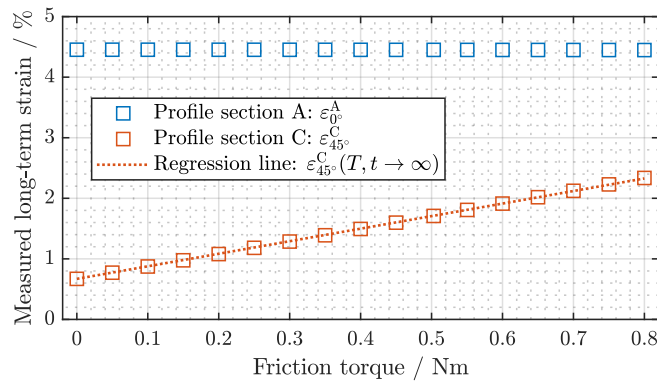

Figure 9: Friction torque-dependent measured long-term strain at profile sections A and C corresponding to long-term material behavior ($t \to \infty$)

According to Figure 9, the measured long-term strain at profile section A due to assembly deformation $\varepsilon_{0°}^{A}(t \to \infty)$ can be acquired regardless of the prevailing friction torque, as its contribution is smaller than the scatter caused by numerical deviations in the model.

At profile section C, on the other hand, the influence of shear deformation is again described in a linear relationship with friction torque T by the measured long-term strain $\varepsilon_{45°}^{C}(T, t \to \infty)$ starting from the assembly strain $\varepsilon_{45°}^{C}(0\,\text{Nm}, t \to \infty)$. The regression line shown in Figure 9 provides a first empirical relationship (3) usable for friction torque determination between operational state and measured long-term strain by means of the long-term proportionality constant c_{LT}.

$$\varepsilon_{45°}^{C}(T, t \to \infty) = \varepsilon_{45°}^{C}(0\,\text{Nm}, t \to \infty) + c_{LT} \cdot T \tag{3}$$

In a future implementation, assembly strain $\varepsilon_{45°}^{C}(0\,\text{Nm}, t \to \infty)$ and rise factor c_{LT} are to be determined empirically in a long-term test in order to include additional contributions to the system behavior due to manufacturing tolerances or mechanical interaction between RSS and strain gauge. Furthermore, technical applicability requires knowledge of the time-dependent rubber behavior, which is examined in Section 4.3.

4.3   Compensation for relaxation and retardation

Based on a hyperelastic material model, a strain-based concept for measurement of friction torque (profile section C) as well as preload (profile section A) as central operational parameters was introduced. However, due to rubber relaxation and its retardation (see Section 2), a time-dependent drift of the measurement signal is to be expected in reality, which is quantified using hyper-viscoelastic material modelling below.

In Figure 10, the measured strains in torque-free state II are plotted over the time elapsed since RSS assembly on the shaft.
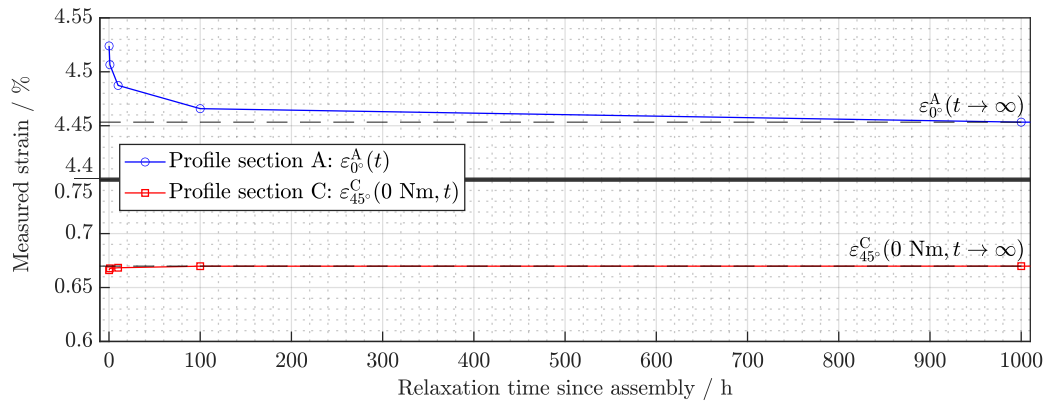
Figure 10: Time-dependent measured strain on profile section A and C due to assembly deformation

The measured strain on profile section A $\varepsilon_{0°}^{A}(t)$ initially decreases rapidly and strives towards its long-term value $\varepsilon_{0°}^{A}(t \to \infty)$ as the relaxation time progresses. The relative deviation of a measurement from measured long-term strain $\varepsilon_{0°}^{A}(t)/\varepsilon_{0°}^{A}(t \to \infty)$ after 0.1 hours (= 6 minutes) of relaxation amounts 1.6%. A similar progression in a smaller extent on profile section C analogously leads to the measurement error $\varepsilon_{45°}^{C}(t)/\varepsilon_{45°}^{C}(t \to \infty)$ = -0.6%. Thus, under the boundary conditions selected here an influence of relaxation on the measured assembly deformation can be neglected and the time-dependent assembly strain $\varepsilon_{45°}^{C}(0 \text{ Nm}, t)$ can still be considered constant (4) with small error.

$$\varepsilon_{45°}^{C}(0 \text{ Nm}, t) \approx \varepsilon_{45°}^{C}(0 \text{ Nm}, t \to \infty) = \varepsilon_{45°}^{C,\text{Offset}} \tag{4}$$

Should it become necessary to include relaxation mechanisms in the future, for example due to their temperature-induced increase, compensation in the measurement signal could be carried out based on the time elapsed since assembly. In the following, however, based on assumption (4), the assembly strain $\varepsilon_{45°}^{C,\text{Offset}}$ is subtracted from the measured strain $\varepsilon_{45°}^{C}(T, t)$ according to equation (5), so that the adjusted measured strain $\tilde{\varepsilon}_{45°}^{C}(T, t)$ results.

$$\tilde{\varepsilon}_{45°}^{C}(T, t) = \varepsilon_{45°}^{C}(T, t) - \varepsilon_{45°}^{C,\text{Offset}} \tag{5}$$

In contrast to profile section A, the operational state III applies a force-controlled deformation to profile section C inducing the rubber to creep (compare Section 2). According to the operational conditions displayed in Figure 11 (left), this is reflected by a significant time dependency of the measured strain. Beginning at the time of friction torque application ($t = 0$ h), strain increases logarithmically until after approximately 1000 h the long-term state known from Section 4.2 is reached.
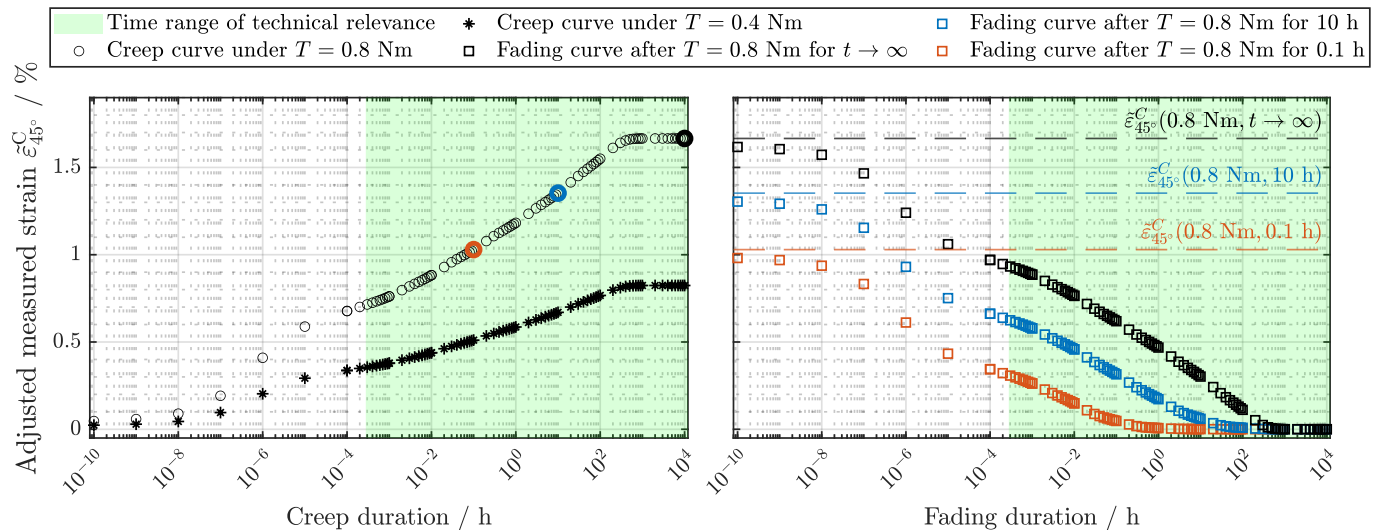

Figure 11: Time-dependency of adjusted measured strain at profile section C $\tilde{\varepsilon}_{45°}^{C}(T, t)$ under application (left) and removal (right) of friction torque

The comparison of two different operating conditions ($T = 0.4$ Nm and $T = 0.8$ Nm) in Figure 11 (left) clearly demonstrates, that the time-strain curve is predefined through the creep modulus as a material property [20] and scaled by the prevailing friction torque in the same way as the measured long-term strain. This analogously applies to the strain's fading process shown in Figure 11 (right), which was simulated by removing the friction torque ($T = 0.8$ Nm) from the FE model after the operational state III. During this process, the linear viscoelastic material model reduces the measured strain back to the original state with a time delay. If the long-term strain was reached in the previous operational state, the fading curve (black) corresponds to the inversion of the creep curve passed before. However, if the creep process is terminated prematurely (after 10 h, blue, and after 0.1 h, red), the fading curve's

start strain shifts according to the previously reached level and thus ends approximately after the same duration as the creep which preceded.

Of technical relevance in the creeping and fading behavior introduced are those time decades which are shaded in green in Figure 11 and can be recorded with the intended sample rate of 1 Hz. Independently of the friction torque, the relative error between the adjusted measured long-term strain and the first measurement is $(\tilde{\varepsilon}_{45°}^{C}(T, t \to \infty) - \tilde{\varepsilon}_{45°}^{C}(T, 1\,\text{s}))/\tilde{\varepsilon}_{45°}^{C}(T, t \to \infty) = 57\%$, which will be the reason for the compensation for the rubber's retardation behavior to represent the main challenge when processing future measurement signals.

At first, a time-independent mathematical description of the creep curves as a function of friction torque is required. In order to make the prevailing friction torque accessible from adjusted measured strain without processing any previous strain curve, a further parameter is needed. For this purpose, the strain rate $\dot{\tilde{\varepsilon}}_{45°}^{C}$ is suitable, which is related with the prevailing stress [14] and as the time derivative of the measured strain accessible by means of the differential quotient. The combination of both variables can now be unambiguously mapped along the creep curves of Figure 11 (left) to the striven long-term strain. Therefore, point sets of adjusted measured strain and strain rate can be drawn as a locus curve, as shown in Figure 12 (left) for four different operating conditions over the technically relevant range.
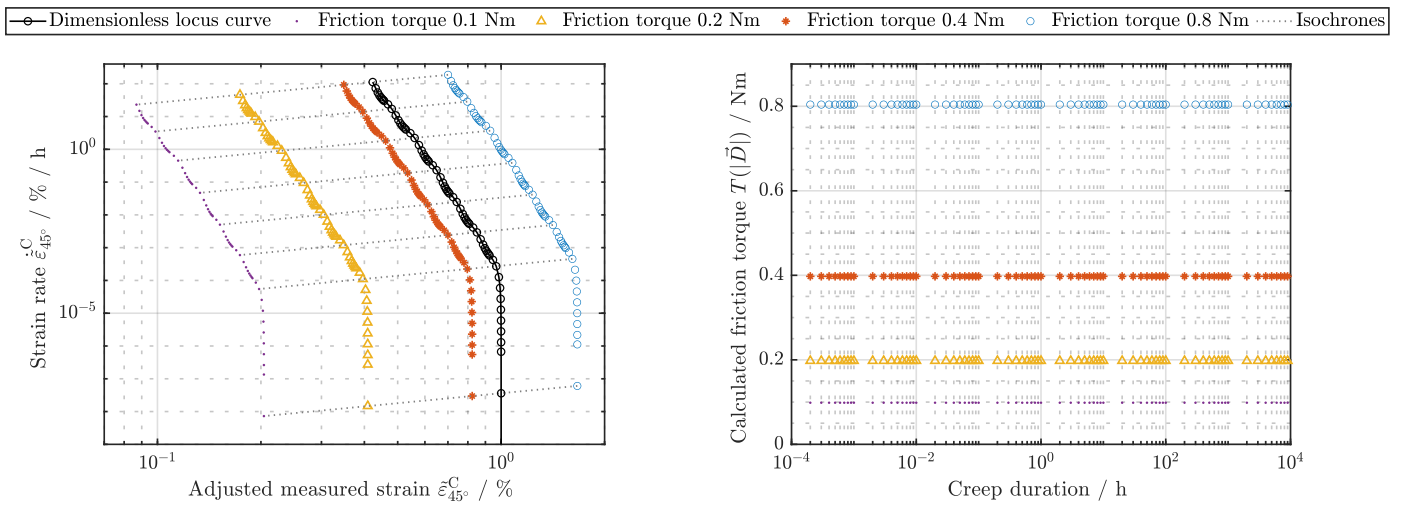

Figure 12: Locus curve consisting of adjusted measured strain $\tilde{\varepsilon}_{45°}^{C}$ and strain rate $\dot{\tilde{\varepsilon}}_{45°}^{C}$ dimensionless (black) as well as scaled to four different operational states (left) and friction torque T determined pointwise by isochrone length (right)

The resulting locus curves with creep duration as a point set parameter each reflect the rubber's retardation behavior and are therefore congruent. The friction torque-dependent scaling of the locus curve due to the double logarithmic representation selected in Figure 12 (left) corresponds exclusively to a locus curve displacement $\vec{D}(T)$ along both axes, as verified by term (6).

$$\begin{pmatrix} \log_{10}\left(\tilde{\varepsilon}_{45°}^{C}(T,t) \cdot (d_1(T))\right) \\ \log_{10}\left(\dot{\tilde{\varepsilon}}_{45°}^{C}(T,t) \cdot (d_2(T))\right) \end{pmatrix} = \begin{pmatrix} \log_{10}(d_1(T)) \\ \log_{10}(d_2(T)) \end{pmatrix} + \begin{pmatrix} \log_{10}\left(\tilde{\varepsilon}_{45°}^{C}(T,t)\right) \\ \log_{10}\left(\dot{\tilde{\varepsilon}}_{45°}^{C}(T,t)\right) \end{pmatrix} = \vec{D}(T) + \begin{pmatrix} \log_{10}\left(\tilde{\varepsilon}_{45°}^{C}(T,t)\right) \\ \log_{10}\left(\dot{\tilde{\varepsilon}}_{45°}^{C}(T,t)\right) \end{pmatrix} \quad (6)$$

Thus, all possible operating conditions with constant set parameter t^* span an isochrone as a line of equal creep duration, as visualized in grey in Figure 12 (left) for several logarithmically spaced time points. This relationship can be used to determine the friction torque by relating to a reference curve. For this purpose, an arbitrary locus curve (selected here: 0.8 Nm) is normalized to the long-term state in both dimensions. This division of adjusted measured strain $\tilde{\varepsilon}_{45°}^{C}(0.8\,\text{Nm}, t)$ as well as strain rate $\dot{\tilde{\varepsilon}}_{45°}^{C}(0.8\,\text{Nm}, t)$ by the corresponding long-term strain $\tilde{\varepsilon}_{45°}^{C}(0.8\,\text{Nm}, t \to \infty)$ results in the dimensionless locus curve shown in Figure 12 (left, black graph), which is no longer dependent on friction torque and thus ends in the dimensionless strain 1.

By spanning an isochrone between the dimensionless and a scaled case, a connection between long-term strain and locus curve displacement $\vec{D}(T)$ is now given by equation (7).

$$\begin{pmatrix} \log_{10}\left(\tilde{\varepsilon}_{45°}^{C}(T,t^*)/\tilde{\varepsilon}_{45°}^{C}(T,t \to \infty)\right) \\ \log_{10}\left(\dot{\tilde{\varepsilon}}_{45°}^{C}(T,t^*)/\tilde{\varepsilon}_{45°}^{C}(T,t \to \infty)\right) \end{pmatrix} \overset{(4)}{=} \vec{D}(T) + \begin{pmatrix} \log_{10}\left(\tilde{\varepsilon}_{45°}^{C}(T,t^*)\right) \\ \log_{10}\left(\dot{\tilde{\varepsilon}}_{45°}^{C}(T,t^*)\right) \end{pmatrix} \quad (7)$$

Substituting the long-term torque-strain correlation from equation (3) (see Section 4.2), the relationship between friction torque and locus displacement ($T \mapsto \vec{D}$) is obtained from equation (8).

$$\Rightarrow \vec{D}(T) = \begin{pmatrix} \log_{10}\left(1/\tilde{\varepsilon}_{45°}^{C}(T,t \to \infty)\right) \\ \log_{10}\left(1/\tilde{\varepsilon}_{45°}^{C}(T,t \to \infty)\right) \end{pmatrix} \overset{(1)}{=} \begin{pmatrix} \log_{10}(1/(c_{LT} \cdot T)) \\ \log_{10}(1/(c_{LT} \cdot T)) \end{pmatrix} \quad (8)$$

Due to identical displacement components $d_1(T) = d_2(T)$ Equation (8) makes apparent that all isochrones run parallel and in the direction of the diagram's bisector. Therefore, a linear line with an angle of 45° (or -45°) can be constructed starting from an arbitrary system state $(\bar{\varepsilon}_{45°}^C, \dot{\bar{\varepsilon}}_{45°}^C)$ in order to determine its point of intersection with the dimensionless locus curve. With knowledge of IMG displacement vector $\vec{D}$, from its magnitude as the isochrone length the friction torque $T(|\vec{D}|)$ results according to equation (8).

$$T(|\vec{D}|) = \frac{1}{c_{Lz}} \cdot 10^{\frac{|\vec{D}|}{\sqrt{2}}} \tag{9}$$

The result of a friction torque calculation using the locus curve method suggested is plotted in Figure 12 (right) over creep time for the simulated strain curves. The relative error between calculated and actually applied friction torque $(T - T(|\vec{D}|))/T$ is less than 0.5% for all operational conditions and time points examined. The locus curve method could therefore also serve for future practical implementations based on measured strains, whereby an empirical determination of the dimensionless locus curve in a long-term test should underlie.

However, the validity of this method is still limited to systems without prior operation, as this causes the strain fading behavior demonstrated in Figure 11 (right) and discussed before. Thus, in case of changing friction torque during operation, for example due to shaft speed variation, a delayed readjustment of measured strain and strain rate to their torque-characteristic relationship is to be expected.

To ensure that the locus curve method is also applicable under unsteady operating conditions, the load history preceded must be compensated for in the measured strain. For this, dimensionless reference curves can as well be used, which according to Figure 13 are obtained from the normalization of fading curves at an arbitrary operational state.
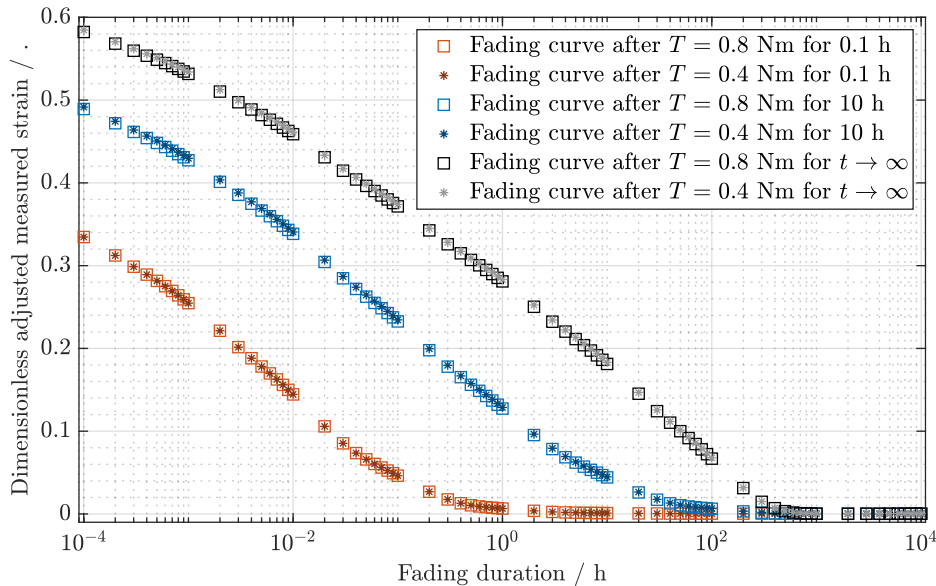

Figure 13: Dimensionless fading curves as time-delayed decrease of measured strain after several preceded creep durations at varied friction torque T

In this case, the fading curves are each normalized to the last prevailing measured strain of the previous operational state, so that curves of equal preceded creep duration are coincident (compare $T = 0.4$ Nm with $T = 0.8$ Nm in Figure 13). In practice, these reference fading curves could allow compensation for any previous operational state in the measurement signal by scaling to the last recorded system state $(\bar{\varepsilon}_{45°}^C, \dot{\bar{\varepsilon}}_{45°}^C)$. An elimination of fading previous states in the measured strain can then be carried out based on the BOLTZMANN superposition principle (c.f. Section 2) by subtraction of the scaled reference curve.

This approach is demonstrated below by means of an exemplary change of operating conditions from $T_1 = 0.3$ Nm after 10 hours (Operational state A) of creep duration to $T_2 = 0.1$ Nm (Operational state B).

As shown in Figure 14, operational state A as the first system stress allows the friction torque $T(|\vec{D}|)$ (red) to be calculated directly from the adjusted measured strain (black) as according to the locus curve method.
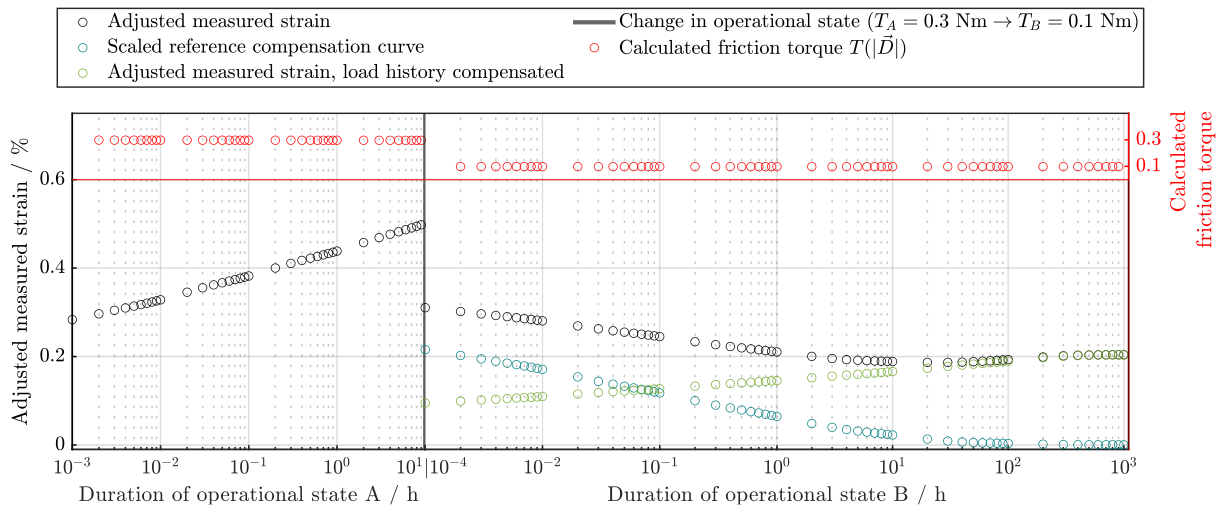
Figure 14: Load history compensation at changing operational conditions after 10 h for friction torque calculation following the locus curve method

Due to the strain level built up after 10 h, a superimposition of the operational state B with fading of operational state A occurs after friction torque alteration. A scaling of the dimensionless fading curve for preceded creep durations of 10 h (compare blue graph in Figure 13) to the final measured strain of operational state A $\bar{\varepsilon}_{45°}^{C}(0.3\ \text{Nm},\ 10\ \text{h})$ delivers the required compensation curve, which is shown in turquoise in Figure 14 and subtracted from the measured strain the next step. The corrected measured strain (Figure 14, green) now corresponds to the torque-characteristic creep curve of operational state B, so that the applied friction torque can finally be determined as $T(|\vec{D}|)$ in any point following the locus curve method.

Thus, by the example of changing operational conditions, it could be demonstrated that creep processes in the measurement signal can be compensated for by examining the superimposition of a present and previous operational states. In the future, the approach presented could be continuously applied to shorter, consecutive time intervals in order to enable the detection of continuous changes in operational state, such as those occurring during the run-in process of an RSS. With a uniform interval width, this decomposition of load history would also reduce the map required for compensation by the dimension of time (c.f. time-dependent reference fading curves in Figure 13). Due to similar creep and fading durations (compare Figure 11 left and right) coupled with the underlying principle of fading memory (c.f. Section 2, [22]), only a limited number of past intervals would have to be taken into account, so that the build-up of integrated errors beyond the sum of interval durations can be excluded.

Based on the in-depth simulative investigation of the sealing system, the presented measuring principle appears promising for first experimental implementation under laboratory conditions. Such tests will be presented in the following part of this paper series focused on manufacturing aspects and several issues neglected until now, particularly the interaction between strain gauge and RSS. This will further provide an outlook on the technical applicability of the calculation methods presented above.

5 Summary and outline

With the long-term aim of developing a new method for in situ condition monitoring of RSS, the presented FE analysis served to identify two potential placements for conventional foil strain gauges that in theory are suitable for strain-based measurement of central operational parameters. From the surface strain occurring along the measuring grid, it was possible to derive measured parameters for evaluation of the rubber's preload connected to radial force and ageing condition as well as the friction torque prevailing in the sealing contact. Furthermore, the time-dependent drift of potential measurement signal resulting from viscoelastic material behavior due to relaxation and retardation mechanisms were investigated. Here, the consideration of creep effects represented a main challenge. A compensation method based on temporary processing of the load history was suggested as a corrective measure and tested simulatively with promising results.

Based on the results obtained, the presented strain-based measurement method for evaluation of operating conditions appears to be theoretically possible. However, an implementation under realistic conditions will require extensions of the presented approach in order to include additional parameters connected to the operational state. In particular, prevailing temperature fields and pressure loads must be taken into account in future investigations.

In the next step, the technical feasibility should be assessed under laboratory conditions accessing a validation of the methods presented. This will be carried out in the following part of this paper series with focus on the challenges of manufacturing and any mechanical interaction between RSS and sensor.

Conflicts of interest - On behalf of all authors, the corresponding author states that there is no conflict of interest.

References

[1]   E. Kirchner, T. Wallmersperger, T. Gwosch, J. D. M. Menning, J. Peters, R. Breimann, B. Kraus, P. Welzbacher, J. Küchenhof, D. Krause, E. Knoll, M. Otto, B. Muhammedi, S. Seltmann, A. Hasse, G. Schäfer, A. Lohrengel, S. Thielen, Y. Stiemcke, O. Koch, A. Ewert, T. Rosenlöcher, B. Schlecht, A. Prokopchuk, E.-F. M. Henke, F. Herbst, S. Matthiesen, D. Riehl, F. Keil, K. Hofmann, F. Pape, D. Konopka, G. Poll, T. Steppeler, R. Ottermann, F. Dencker, M. C. Wurz, S. Puchtler, T. Baszenski, M. Winnertz, G. Jacobs, B. Lehmann and K. Stahl, "A Review on Sensor-integrating Machine Elements," *Advanced Sensor Research, accepted,* 2023.

[2]   S. Thielen, Y. Stiemcke, B. Sauer, O. Koch, P. Sivasothy, J. Seewig and C. Rheinländer, "Sensorintegrierendes Maschinenelement Radialwellendichtring zur Überwachung von Betriebszustand und Schmierstoffqualität," in *Dresdner Maschinenelemente Kolloquium*, 2022.

[3]   R. K. Flitney, Seals and Sealing Handbook, 6 ed., Butterworth-Heinemann, 2014.

[4]   H. K. Mueller and B. S. Nau, Fluid sealing technology, vol. 117, M. Dekker, 1998, p. 485.

[5]   T. Schollmayer, S. Thielen, B. Sauer and O. Koch, "Characterization of radial shaft seal performance in contaminated environments," in *21st International Sealing Conference*, 2022.

[6]   S. Thielen, *Entwicklung eines TEHD-Tribosimulationsmodells für Radialwellendichtringe,* 2019.

[7]   W. B. Dapp, A. Lücke, B. N. J. Persson and M. H. Müser, "Self-Affine Elastic Contacts: Percolation and Leakage," *Physical Review Letters,* vol. 108, p. 244301, June 2012.

[8]   S. Thielen, B. Magyar and B. Sauer, "Thermoelastohydrodynamic Lubrication Simulation of Radial Shaft Sealing Rings," *Journal of Tribology,* vol. 142, January 2020.

[9]   C. Wilbs, D. Frölich, M. Adler and A. Heinl, "Radial lip seal friction torquea suitable lubricant-elastomer compatibility indicator?," in *1st International Conference on Tribology and Sustainable Lubrication*, 2023.

[10]   B. Wennehorst, "On lubrication and friction in soft rough conformal sliding contacts : experimental and theoretical contributions to the discussion on elastomer shaft seal tribology," 2016.

[11]   H. Alexander, M. Wöppermann and J. Hermes, "Dynamische RWDR Tests neu definiert!," *Tribologie und Schmierungstechnik,* vol. 67, 2020.

[12]   M. Schulz, M. Baumann and F. Bauer, "Influence of Different Shaft Surface Finishes on the Lubrication and Friction Condition of Elastomeric Lip Seals," in *Proceedings IRF2020: 7th International Conference Integrity-Reliability-Failure*, 2020.

[13]   L. R. G. Treloar, The Physiscs of Rubber Elastocity, Oxford University Press, 1975.

[14]   M. Stommel, M. Stojek and W. Korte, FEM zur Berechnung von Kunststoff- und Elastomerbauteilen, 2 ed., Carl Hanser Verlag München, 2018.

[15]   M. Mooney, "A Theory of Large Elastic Deformation," *Journal of Applied Physics,* vol. 11, p. 582–592, September 1940.

[16]   R. S. Rivlin, "Large elastic deformations of isotropic materials IV. further developments of the general theory," *Philosophical Transactions of the Royal Society of London. Series A, Mathematical and Physical Sciences,* vol. 241, p. 379–397, October 1948.

[17]   I. Doghri, Mechanics of Deformable Solids, Springer Berlin Heidelberg, 2000.

[18]   U. Eisele, Introduction to Polymer Physics, Springer Berlin Heidelberg, 1990.

[19]   U. Mohr-Matuschek, *Auslegung von Kunststoff- und Elastomerformteilen mittels Finite-Elemente-Simulationen,* 1991.

[20]   F. R. Schwarzl, Polymermechanik, Springer Berlin Heidelberg, 1990.

[21]   N. W. Tschoegl, The Phenomenological Theory of Linear Viscoelastic Behavior, Springer Berlin Heidelberg, 1989.

[22]   B. D. Coleman and W. Noll, "Erratum: Foundations of Linear Viscoelasticity," *Reviews of Modern Physics,* vol. 36, p. 1103–1103, October 1964.

[23]   M. Achenbach and M. Herdy, "Mit Evolutionsstrategie viskoelastische

Materialparameter aus thermorheologischen Messwerten ermitteln," *KGK Kautschuk, Gummi, Kunststoffe,* vol. 56. Jahrgang, pp. 24-31, February 2003.

[24]   B. Fazekas, C. Burkhart, S. Staub, S. Thielen, H. Andrä, T. J. Goda, B. Sauer and O. Koch, "Radial shaft seals: How ageing in oil and hyper-viscoelasticity affect the radial force and the numerically predicted wear," *Tribology International,* vol. 186, p. 108601, August 2023.

[25]   C. Burkhart, *Ein Beitrag zum Verständnis des Verschleißverhaltens im System Radialwellendichtring,* 2022.

[26]   *DIN 3761-8:1984-01, Rotary shaft lip type seals for automobils; test; carrying out axle-sections.*

[27]   D. Frölich, *Strategien und Modelle zur Simulation des Betriebsverhaltens von Radial-Wellendichtringen,* 2016.

[28]   D. Frölich, B. Magyar and B. Sauer, "A comprehensive model of wear, friction and contact temperature in radial shaft seals," *Wear,* vol. 311, p. 71–80, March 2014.

[29]   T. Leichner, *Prognose der Dichtlippenfolgefähigkeit von RWDR bei dynamisch verlagerter Welle,* 2012.

[30]   *DIN 3761:-91984-01, Rotary shaft lip type seals for automobils; test; radial force measuring instrument digital.*

[31]   T. Schollmayer, C. Burkhart, W. Kassem, S. Thielen and B. Sauer, "Verschleiß analyse an Radialwellendichtringen und weiteren Maschinenelementen mittels Laserprofilometrie," *Gesellschaft für Tribologie e.V. (Hg.): 62. Tribologie-Fachtagung,* vol. 62, pp. 70/1-70/10, 2021.

[32]   D. Gross, W. Hauger, J. Schröder and W. A. Wall, Technische Mechanik 2: Elastostatik, Springer Berlin Heidelberg, 2014.

[33]   R. Bandorf, H. Gerdes, U. Heckmann, G. Bräuer and M. Petersen, "4.1.3 Hochempfindliche Dünnschicht-Dehnungsmessstreifen auf technischen Bauteilen," in *Tagungsband*, 2012.

[34]   O. A. Araromi, M. A. Graule, K. L. Dorsey, S. Castellanos, J. R. Foster, W.-H. Hsu, A. E. Passy, J. J. Vlassak, J. C. Weaver, C. J. Walsh and R. J. Wood, "Ultra-sensitive and resilient compliant strain gauges for soft machines," *Nature,* vol. 587, p. 219–224, November 2020.

[35]   Y. Stiemcke, S. Thielen, T. Schollmayer and O. Koch, "Investigation of the effect of underpressure between main and dust lip on the performance of radial shaft seals under instationary shaft movements," *Journal of Tribology,* p. 1–18, January 2024.

[36]   S. Keil, Dehnungsmessstreifen, Springer Fachmedien Wiesbaden, 2017.

[37]   Freudenberg Sealing Technologies, *Technisches Handbuch - Ausgabe 1,* 2015.

[38]   K. Hoffmann, Eine Einführung in die Technik des Messens mit Dehnungsmessstreifen, Hottinger Baldwin Messtechnik GmbH, 1987.